OPEN ACCESS

Japanese Journal of Applied Physics **58**, SCCB18 (2019) **REGULAR PAPER**

https://doi.org/10.7567/1347-4065/ab147a

Influence of InN and AlN concentration on the compositional inhomogeneity and formation of InN-rich regions in $In_xAl_yGa_{1-x-y}N$

Gunnar Kusch[1*], Johannes Enslin[2], Lucia Spasevski[1], Tolga Teke[2], Tim Wernicke[2], Paul R. Edwards[1], Michael Kneissl[2], and Robert W. Martin[1]

[1]*Department of Physics, SUPA, University of Strathclyde, Glasgow G4 0NG, United Kingdom*
[2]*Technische Universität Berlin, Institut für Festkörperphysik, Hardenbergstr. 36, EW 6-1, 10623 Berlin, Germany*

[*]E-mail: gk419@cam.ac.uk

Received January 1, 2019; accepted March 5, 2019; published online May 14, 2019

The application of quaternary $In_xAl_yGa_{1-x-y}N$ active regions is a promising path towards high efficiency UVB-light emitting diodes (LEDs). For the utilization of $In_xAl_yGa_{1-x-y}N$, detailed knowledge of the interplay between growth parameters, adatom incorporation, optical and structural properties is crucial. We investigated the influence of the trimethylaluminium (TMAl) and trimethylindium (TMIn) flux on the composition and luminescence properties of $In_xAl_yGa_{1-x-y}N$ layers by multi-mode scanning electron microscopy. We found that varying the molar TMIn flow from 0 to 17.3 μmol min^{-1} led to an InN concentration between 0% and 3.2% and an emission energy between 4.17 and 3.75 eV. The variation of the molar TMAl flow from 3.5 to 35.4 μmol min^{-1} resulted in a AlN composition between 7.8% and 30.7% with an emission energy variation between 3.6 and 4.1 eV. Cathodoluminescence hyperspectral imaging provided evidence for the formation of nanoscale InN-rich regions. Analyzing the emission properties of these InN-rich regions showed that their emission energy is inhomogeneous and varies by ≈150 meV. We provide evidence that the formation of these InN-rich regions is highly dependent on the AlN and InN composition of the layer and that their formation will strongly affect the performance of $In_xAl_yGa_{1-x-y}N$ LEDs. © 2019 The Japan Society of Applied Physics

1. Introduction

Ultraviolet (UV) light emitting diodes (LEDs) in the UVB wavelength region show potential for applications including: UV-curing, gas-sensing and photo-therapy of, for example, psoriasis.[1–3] However, the external quantum efficiency (EQE) of UVB emitting devices is not high enough to satisfy the demands of these commercial applications, exhibiting EQE values even lower than UV-C LEDs.[3] There are indications that the internal quantum efficiency of UVB emitting quantum wells (QWs) can be increased by replacing the conventionally used ternary AlGaN/AlGaN QW/quantum barrier (QB) active region with a QW structure based on the quaternary $In_xAl_yGa_{1-x-y}N$ alloy.[4,5] This was attributed to In segregation effects, creating areas with higher InN fractions, leading to enhanced carrier localization and an increased electron hole overlap, analogous to the InGaN case.[6–8] Currently a lack of understanding of the incorporation, segregation and phase separation mechanisms[9,10] of InN in $In_xAl_yGa_{1-x-y}N$ is a barrier to the full utilization of the beneficial properties of $In_xAl_yGa_{1-x-y}N$ for the growth and fabrication of UVB LEDs. Understanding the incorporation of InN is crucial for the design of optical devices for applications like gas-sensing, utilizing narrow wavelength windows.

In this paper we investigate the influence of the trimethylindium (TMIn) and trimethylaluminium (TMAl) fluxes during growth of $In_xAl_yGa_{1-x-y}N$ layers on their optical, morphological and compositional properties in order to further understand the optical quality and compositional homogeneity. We correlate these different properties by utilizing multiple signals generated by a beam of high energy electrons in an SEM, allowing us to investigate the optical properties via cathodoluminescence (CL) hyperspectral imaging,[11,12] the morphology by secondary electron (SE) imaging and the composition by wavelength dispersive X-ray (WDX) spectroscopy.

2. Experimental

Two sample series were grown, on *c*-plane AlN/Al_2O_3 templates, using an 3×2 inch close-coupled showerhead metalorganic vapor phase reactor. Triethylgallium (TEGa), TMAl, TMIn and ammonia (NH_3) were used as precursors, while the carrier gas was nitrogen. The samples consist of a nominally undoped (In)AlGaN layer with a nominal thickness of 150 nm grown on top of metamorphic $Al_{0.5}Ga_{0.5}N$ on AlN/sapphire; more information on the growth of the $Al_{0.5}Ga_{0.5}N$:Si on AlN/sapphire can be found in work published by Ref. 13. For the first sample series the molar TMIn flow rate in the gas phase was varied between 0 and 17.3 μmol min^{-1} while the growth temperature (824 °C ± 2 °C), the reactor pressure (400 mbar) as well as the TMAl (26.5 μmol min^{-1}), TEGa (8.9 μmol min^{-1}) and NH_3 (89.4 mmol min^{-1}) flow were kept constant. In the second growth series the molar TMAl flow in the gas phase was varied between 3.5 and 35.4 μmol min^{-1} with the growth temperature (828 °C ± 2 °C), the reactor pressure (400 mbar), TMIn (17.3 μmol min^{-1}), TEGa (8.9 μmol min^{-1}) and NH_3 (89.4 mmol/min) flow kept constant. An overview of the TMIn and TMAl flow rates for the two different sample series is given in Table I.

WDX measurements were carried out in a JEOL JXA–8530F electron probe microanalyser to determine the composition of all samples, using AlN, GaN and InP as standards. The measurements were performed with a beam current of 40 nA, 5 kV acceleration voltage and a beam defocused to a spot size of 10 μm. Carbon coating of the samples was necessary as charging effects were observed during initial measurements; coatings similar to the standards were applied to all samples. SE and CL imaging were conducted on uncoated samples in a FEI Quanta 250 environmental

Table I. Overview of the investigated samples, note that sample 1 is the same for both series. The composition values of sample 6 are not included as the WDX weight total of the WDX measurement diverged too far from 100%.

Sample	TMIn flow [μmol min^{-1}]	TMAl flow [μmol min^{-1}]	InN [%]	AlN [%]	CL NBE emission energy [eV]	Extra CL peak [eV]
1	17.3	26.5	1.96 ± 0.06	17.6 ± 0.4	3.75	
2	8.7	26.5	3.20 ± 0.10	28.8 ± 0.7	3.93	x
3	4.2	26.5	1.82 ± 0.09	30.5 ± 0.7	3.99	x
4	0	26.5	0	34.0 ± 0.7	4.17	
5	17.3	35.4	1.87 ± 0.07	30.7 ± 0.7	4.06	x
1	17.3	26.5	1.96 ± 0.06	17.6 ± 0.4	3.75	
6	17.3	14.1			3.68	
7	17.3	8.7	1.38 ± 0.04	11.5 ± 0.3	3.67	
8	17.3	3.5	1.25 ± 0.04	07.8 ± 0.2	3.60	

scanning electron microscope in high and low vacuum mode, as necessitated by the charging of the samples.[14] CL spectra and hyperspectral images were acquired with a spectrometer with a focal length of 125 mm with 600 l mm^{-1} gratings blazed at 200 nm and 400 nm, a 50 μm entrance slit and a 1600-element charge-coupled device. The measurements where performed at room temperature with an acceleration voltage of 5 kV and a beam current of 2.9 nA. According to Monte Carlo simulations using CASINO software,[15] approximately 90% of the beam energy is deposited in the first 80 nm of an $Al_{0.35}Ga_{0.65}N$ layer at the chosen acceleration voltage. The sample is tilted by 45° with respect to the electron beam and the generated light is collected by a reflecting objective with its optical axis perpendicular to the electron beam as described by Ref. 16.

3. Results and discussion

CL spectra acquired for all samples show a decrease in the energy of the near band edge (NBE) emission with either an increasing In flux or a decreasing Al flux (Fig. 1), following the trend observed by Ref. 17. By increasing the In flux [shown in Fig. 1(a)] NBE emission energies of 4.17 eV (0 μmol min^{-1}), 3.99 eV (4.2 μmol min^{-1}), 3.93 (8.7 μmol min^{-1}) and 3.75 eV (17.3 μmol min^{-1}) were found. This corresponds to a total redshift of 420 meV. The composition of these samples was determined by WDX. The InN concentration increased with increasing TMIn flux from 0% (0 μmol min^{-1}) to 2% (17.3 μmol min^{-1}) with a maximum concentration at 3.2% (8.7 μmol min^{-1}) while the Al concentration decreases with increasing TMIn flux from 34% (0 μmol min^{-1}) to 17.6% (17.3 μmol min^{-1}). All WDX results are shown in Table I (samples 1–4). The decrease of the InN of the sample with the highest TMIn flow rate is surprising at first. The decrease in InN concentration is accompanied by a strong reduction of the AlN mole fraction (28.8% for 8.7 μmol min^{-1} to 17.6% for 17.3 μmol min^{-1} TMIn) and an according increase of the GaN content. Reference 18 showed that In-radicals can decompose Ga-containing residues on the showerhead, resulting in an increased Ga-incorporation. By increasing the In supply, more radicals can be formed leading to a higher incorporation of Ga and therefore a lower incorporation of In and Al. An additional spectral feature can be observed in the two samples which show high concentration for both InN and AlN (samples 2 and 3), both of which display a low intensity peak that emits at a lower energy than the NBE by 300 ± 10 meV (peak position at 3.69 eV and 3.64 eV for 4.2 μmol min^{-1} and 8.7 μmol min^{-1} respectively).

Increasing the TMAl flux while keeping the TMIn flux constant leads, as expected, to an increase in the AlN concentration and thus a blue shift of the NBE emission energy [Fig. 1(b)]. In this series of samples the NBE shifts by 460 meV from 3.6 eV (3.5 μmol min^{-1}) to 4.06 eV (35.4 μmol min^{-1}). The composition of the samples has been determined by WDX. The InN concentration increases from 1.3% (3.5 μmol min^{-1}) to 1.9% (35.4 μmol min^{-1}) with a maximum of 2.0% at (26.5 μmol min^{-1}) and the AlN concentration increases from 7.8% (3.5 μmol min^{-1}) to 30.7% (35.4 μmol min^{-1}), all results are shown in Table I (samples 1, 5–8), the WDX results for sample 6 are not included as the WDX weight total diverged too far from 100%. The sample with the highest AlN concentration (sample 5) shows an additional spectral feature at an emission energy lower than the NBE, similar to samples 2 and 3 in the TMIn flux series. In comparison to the additional spectral features observed in the TMIn flux series, the emission peak is rather broad, covering an emission range from ≈3.55 to ≈3.90 eV, and much weaker compared to the NBE emission.

In order to investigate the luminescence we compare CL hyperspectral images and SE images. The CL maps for sample 5 of the TMAl flux series, as well as a representative SE-image from a different area of the sample, are shown in Fig. 2. The NBE intensity as well as its peak position were extracted from the hyperspectral dataset by fitting a Lorentzian peak to the NBE peak at each point of the acquired map. The intensity of the additional peak was extracted by applying a digital bandpass to the hyperspectral dataset, showing only the emission energy between 3.55 and 3.90 eV.

The sample morphology [Fig. 2(a)] reveals a high density of surface defects which can be divided into two broad groups: V-pits and trench defects (marked by blue and red arrows in Fig. 2(a) respectively). V-pits commonly form in this material system at threading dislocations, which can act as non-radiative recombination centers.[19] Trench defects were already observed in InGaN[20] and were found to be caused by the presence of basal plane stacking faults that are terminated by stacking mismatch boundaries.[21] In contrast to some findings on trench defects we do not observe an increased luminescence intensity correlated to any of the observed trench defects but only a reduction in intensity [see Fig. 2(b)].[22,23] The high density of these two surface defects is most likely due to the low growth temperature of the $In_xAl_yGa_{1-x-y}N$ layers, as a strong correlation between growth temperature and the formation of trench defects, as well as V-pits, was found in a previous study by Ref. 24.

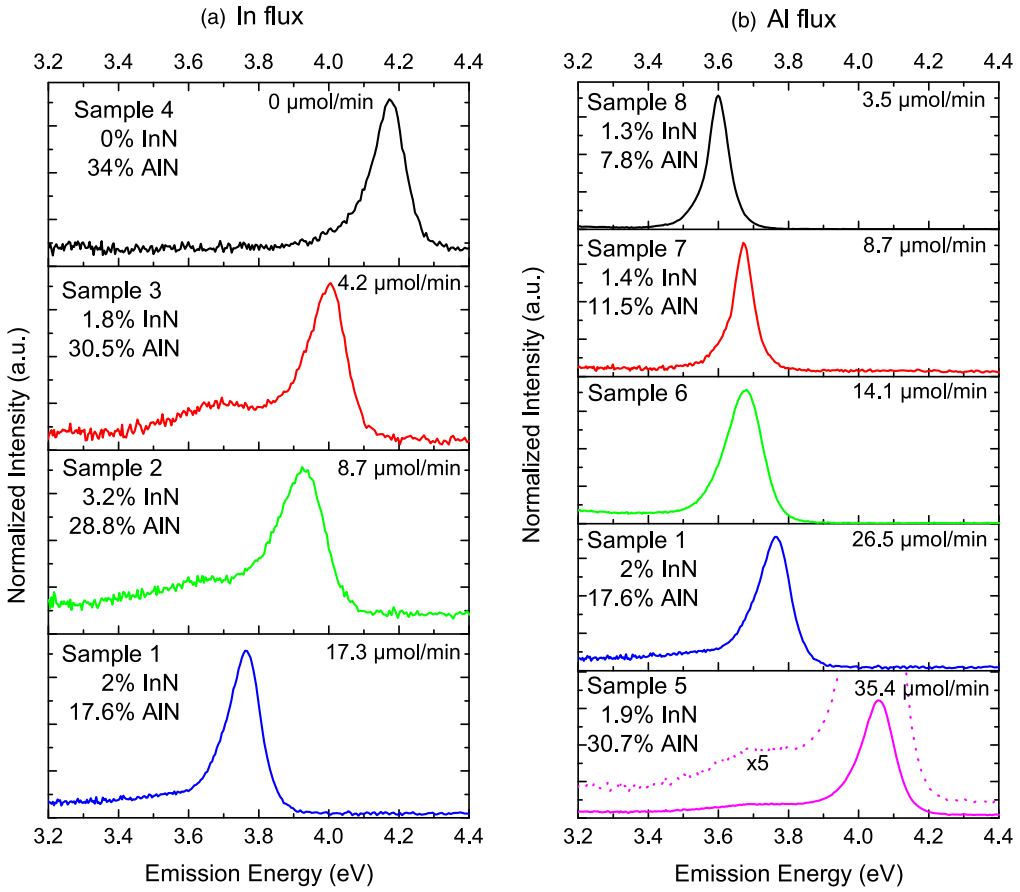

Fig. 1. (Color online) Room temperature CL spectra of the TMIn and TMAl flux sample series. A clear redshift of the NBE emission energy with increasing TMIn flux (a) as well as a clear blue shift of the NBE emission energy with increasing TMAl flux (b) can be observed. An additional low energy peak can be observed for samples 2, 3 and 5.

The NBE intensity map [Fig. 2(b)] shows a strong reduction in emission intensity at the locations where surface defects were observed in the SE-image of the mapped area (not shown) and a fairly homogeneous intensity distribution in between. The NBE emission energy map [Fig. 2(c)] reveals a redshift of up to 30 meV at the location of these surface defects (marked with circles) and a smaller variation in the emission energy of about 10 meV in the areas unperturbed by the surface defects. The redshift at the surface defects is possibly caused by an enhanced InN incorporation in these V-pits and trench defects, as previously observed.[19,22,23,25] The emission energy variation in the rest of the imaged area is most likely caused by small lateral composition inhomogeneities of the quaternary alloy. In contrast to the map of the NBE emission intensity, that of the additional low energy peak [Fig. 2(d)] shows strong spatial variations with clearly observable centers of high emission intensity (marked with arrows). These centers do not correlate with any of the observed surface defects or a decrease in NBE emission intensity.

In Fig. 3 (taken on a different area of sample 5, showing the same behavior), it can be seen that that the emission energy is not homogeneous but varies between each of the different spots. Furthermore, we find that the spatial dimension of these centers of low emission energies is highly localized with a size in the order of 50 nm, or below. We, again, found no correlation between the surface defects and the location of these centers of high emission intensity; which together with the variation in CL peak position shown in Fig. 3, strongly indicates that the effect causing these additional luminescence peaks is related to highly localized variations in the composition of the quaternary layer. The variation in emission energy between the different localized emission centers, is likely caused by their random formation in which different InN-rich regions will have different compositions as well as different sizes and thus different band gap energies.

The formation of nanoscale InN-rich regions in $In_xAl_yGa_{1-x-y}N$ layers has been reported previously by Ref. 26. They investigated the compositional homogeneity and the formation of nanoscale InN-rich regions as a function of temperature, and reported stronger compositional inhomogeneity occurring at lower growth temperatures due to higher InN concentrations. High resolution transmission electron microscopy imaging of their samples revealed that these InN-rich regions are quantum dot like structures forming on a nanometre scale with a size of about 3 nm. Additionally, they were able to observe the appearance of an additional low energy peak in their photoluminescence (PL) spectra in the sample with the highest InN fraction, similar to the observations made in this study. However, they were not able to directly link the additional peak to spatially localized emission centers, owing to the low spatial resolution of PL, whereas in the samples investigated here the correlation is evident.

The samples investigated in our study were grown with a constant growth temperature and show a strong correlation between the formation of localized InN-rich regions and their

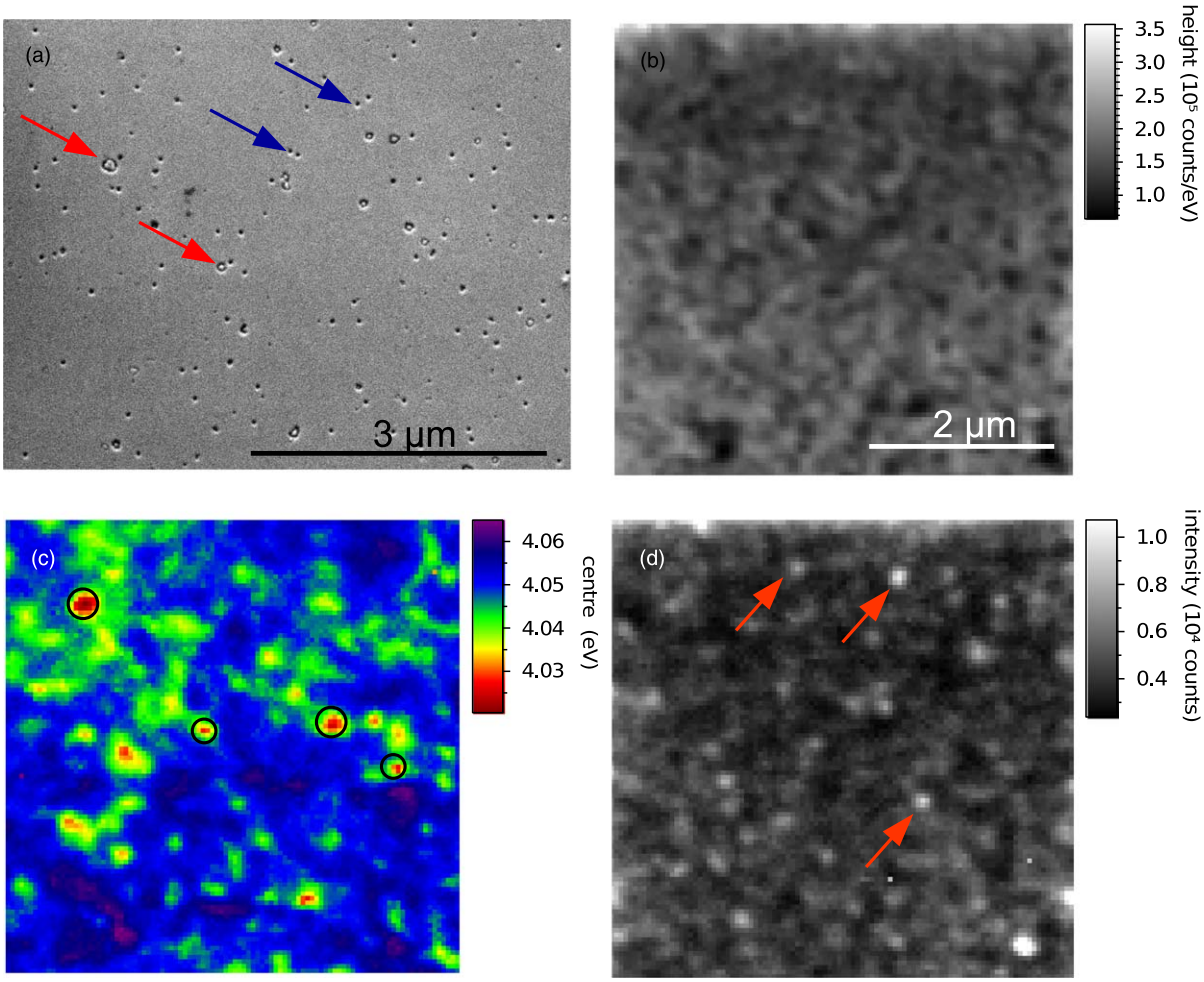

Fig. 2. (Color online) (a) Representative SE-image of the sample surface, (b) fitted NBE CL intensity, (c) NBE CL emission energy and (d) emission intensity between 3.55 and 3.90 eV. The scale bar of the first CL map (b) applies to all shown CL maps, the maps were acquired at room temperature.

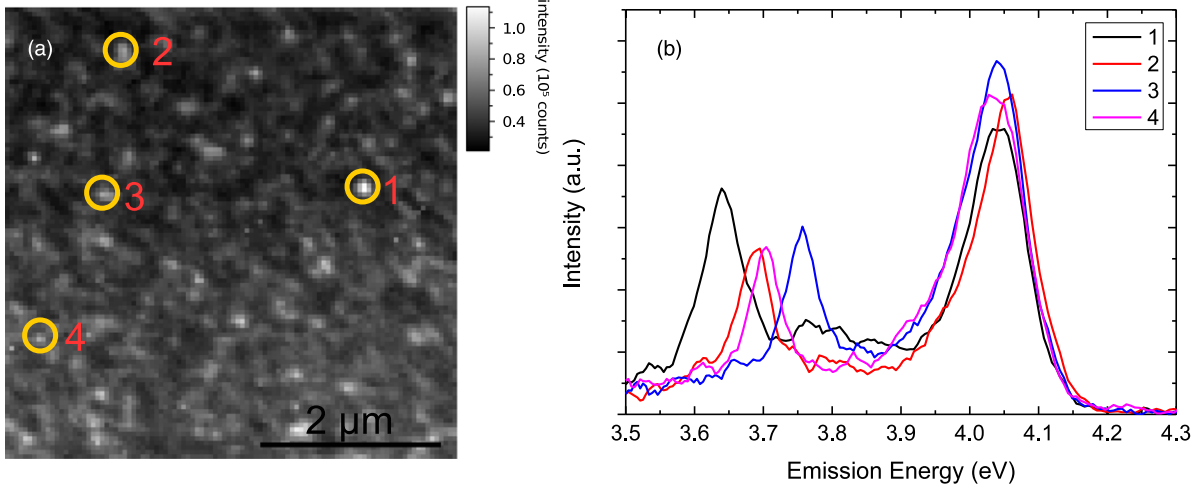

Fig. 3. (Color online) (a) Room temperature CL emission intensity between 3.55 and 3.9 eV, and (b) spectra from four different spots, as marked in (a).

InN and AlN concentrations. Samples with high AlN and InN concentrations show highly localized emission centers (samples 2, 3 and 5 in Table I), while those with high InN and low AlN concentration (sample 1 in Table I) as well as high AlN and no InN (sample 4 in Table I) show none of these centers. This strongly suggest that the interplay between the In and Al atoms causes the formation of small InN-rich regions if a critical concentration of both atomic species has been reached.

These results are summarized in Fig. 4, where each sample is plotted for their InN and AlN mole fractions. The formation of the additional luminescence peaks and their strong spatial localization is marked as red. These additional peaks appear only for high InN and AlN mole fractions. Especially, for a constant InN fraction (samples 1, 5–8 in Table I) in the $In_xAl_yGa_{1-x-y}N$ layer, they do not appear at a low AlN content but they appear at a high AlN content.

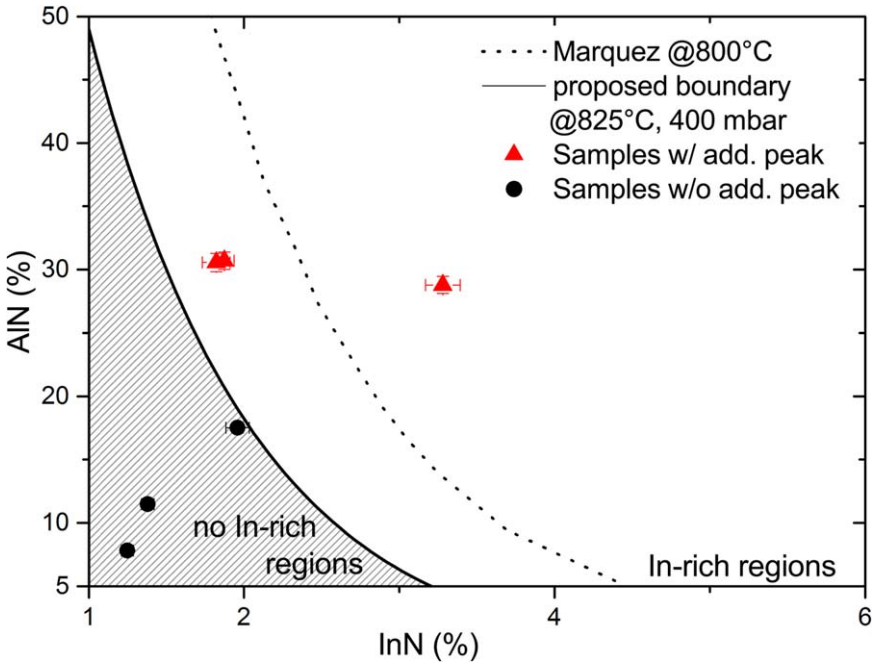

Fig. 4. (Color online) Comparison between this work and theoretical work by Ref. 27 on the no In-rich/In-rich regions boundary for $In_xAl_yGa_{1-x-y}N$. Red points mark samples with an additional emission peak, black points mark sample without an additional peak. The black line is a proposed boundary, translated to 1% lower InN from Ref. 27.

These observations could by explained by theoretical calculations of InN-rich cluster formation by analyzing the thermodynamic stability of quaternary $In_xAl_yGa_{1-x-y}N$.[27] This model analyzes the In–In affinity, which strongly increases with increasing InN and AlN mole fraction, enhancing the formation of In-rich regions. Based on their simulations Marques et al. calculated a boundary line for the formation of InN-rich clusters (for a temperature of 800 °C). In spite of the qualitative agreement, our experimental data (samples 3 and 5, points at 2% InN and 30% AlN in Fig. 4) clearly does not fit to the published simulations (dotted line in Fig. 4). However, these deviations can be explained by the higher growth temperature and parameters not included in the simulation (e.g. strain, reactor pressure, surface reconstruction and surface kinetics). As the model makes reasonable assumptions on the formation of InN-rich clusters, we propose a boundary for the formation of InN-rich clusters at 825 °C and 400 mbar by translating Marques's line to 1% lower InN to match our data (the black line in Fig. 4), which needs more experiments to map out the parameter space.

4. Conclusion

We investigated the influence of the TMIn and TMAl flux on the optical properties of quaternary $In_xAl_yGa_{1-x-y}N$ layers. We found that for certain InN and AlN concentration a second peak at a lower energy than the NBE appears. CL hyperspectral imaging allowed us to identify that the origin of this additional luminescence peak is the formation of spatially highly localized emission centers. Furthermore, we have been able to observe variations in the emission energy as well as intensity from center to center, indicating that these change in size and/or composition. The cause of the appearance of these localized emission centers, as well as their nature, cannot be unambiguously determined but the good agreement between theory and experiment strongly suggest that they are InN-rich regions, forming due to an increase in the In–In affinity. The formation of these InN-rich regions has to be taken into account when utilizing $In_xAl_yGa_{1-x-y}N$ layers for the active region of UV LEDs as they will reduce the spectral purity of devices. However, the occurrence of the InN-rich regions might be exploited on the other hand.

Acknowledgments

We acknowledge funding from the Engineering and Physical Sciences Research Council (EPSRC) (EP/M015181/1 and EP/P02744X/2) of the UK. This work was partially supported by the German Federal Ministry of Education and Research (BMBF) within the "Advanced UV for Life" project and by the Deutsche Forschungsgemeinschaft (DFG) within the Collaborative Research Center "Semiconductor Nanophotonics" (SFB 787). The data associated with this research is available at DOI:https://doi.org/10.15129/e63d2ae4-91a9-4c55-9836-52f8793a3cf6.

1) F. Mehnke et al., IEEE J. Sel. Top. Quantum Electron. **23**, 29 (2017).
2) S. R. Feldman, B. G. Mellen, T. S. Housman, R. E. Fitzpatrick, R. G. Geronemus, P. M. Friedman, D. B. Vasily, and W. L. Morison, J. Am. Acad. Dermatol. **46**, 900 (2002).
3) M. Kneissl and J. Rass, *III-Nitride Ultraviolet Emitters* (Springer International Publishing, Switzerland, 2016).
4) H. Hirayama, J. Appl. Phys. **97**, 091101 (2005).
5) M. Jetter, C. Wächter, A. Meyer, M. Feneberg, K. Thonke, and P. Michler, J. Cryst. Growth **315**, 254 (2011).
6) S. Nakamura, Science **281**, 956 (1998).
7) S. Chichibu, T. Azuhata, T. Sota, and S. Nakamura, Appl. Phys. Lett. **69**, 4188 (1996).
8) K. P. O'Donnell, R. W. Martin, and P. G. Middleton, Phys. Rev. Lett. **82**, 237 (1999).
9) H. Hirayama, A. Kinoshita, T. Yamabi, Y. Enomoto, A. Hirata, T. Araki, Y. Nanishi, and Y. Aoyagi, Appl. Phys. Lett. **80**, 207 (2002).
10) Y. Kobayashi, Y. Yamauchi, and N. Kobayashi, Jpn. J. Appl. Phys. **42**, 2300 (2003).

11) P. R. Edwards, R. W. Martin, K. P. O'Donnell, and I. M. Watson, Phys. Status Solidi C **0**, 2474 (2003).
12) J. Christen, M. Grundmann, and D. Bimberg, J. Vac. Sci. Technol. B **9**, 2358 (1991).
13) J. Enslin et al., J. Cryst. Growth **464**, 185 (2017).
14) G. Kusch, H. Li, P. R. Edwards, J. Bruckbauer, T. C. Sadler, P. J. Parbrook, and R. W. Martin, Appl. Phys. Lett. **104**, 092114 (2014).
15) D. Drouin, A. R. Couture, D. Joly, X. Tastet, V. Aimez, and R. Gauvin, Scanning **29**, 92 (2007).
16) P. R. Edwards, L. K. Jagadamma, J. Bruckbauer, C. Liu, P. Shields, D. Allsopp, T. Wang, and R. W. Martin, Microsc. Microanal. **18**, 1212 (2012).
17) K. Bejtka, P. R. Edwards, R. W. Martin, S. Fernández-Garrido, and E. Calleja, J. Appl. Phys. **104**, 073537 (2008).
18) J. Enslin, T. Wernicke, A. Lobanova, G. Kusch, L. Spasevski, T. Teke, B. Belde, R. W. Martin, R. Talalaev, and M. Kneissl, Jpn. J. Appl. Phys. (submitted).
19) J. P. Liu, Y. T. Wang, H. Yang, D. S. Jiang, U. Jahn, and K. H. Ploog, Appl. Phys. Lett. **84**, 5449 (2004).
20) J. Bruckbauer, P. R. Edwards, T. Wang, and R. W. Martin, Appl. Phys. Lett. **98**, 141908 (2011).
21) F. C.-P. Massabuau, L. Trinh-Xuan, D. Lodié, S.-L. Sahonta, S. Rhode, F. O. E. J. Thrush, M. J. Kappers, C. J. Humphreys, and R. A. Oliver, J. Phys.: Conf. Ser. **471**, 012042 (2013).
22) J. Bruckbauer, P. R. Edwards, S.-L. Sahonta, F. C.-P. Massabuau, M. J. Kappers, C. J. Humphreys, R. A. Oliver, and R. W. Martin, J. Phys. D **47**, 135107 (2014).
23) F. C.-P. Massabuau, L. Trinh-Xuan, D. Lodié, E. J. Thrush, D. Zhu, F. Oehler, T. Zhu, M. J. Kappers, C. J. Humphreys, and R. A. Oliver, J. Appl. Phys. **113**, 073505 (2013).
24) J. Smalc-Koziorowska, E. Grzanka, R. Czernecki, D. Schiavon, and M. Leszczyński, Appl. Phys. Lett. **106**, 101905 (2015).
25) C.-T. Kuo, L.-H. Hsu, Y.-Y. Lai, S.-Y. Cheng, H.-C. Kuo, C.-C. Lin, and Y.-J. Cheng, Appl. Surf. Sci. **405**, 449 (2017).
26) J. Wu et al., Nanotechnology **17**, 1251 (2006).
27) M. Marques, L. K. Teles, L. M. R. Scolfaro, L. G. Ferreira, and J. R. Leite, Phys. Rev. B **70**, 073202 (2004).